Phase transition in the Ruddlesden–Popper layered perovskite Li$_2$SrTa$_2$O$_7$

T. Pagnier [a], N. Rosman [a], C. Galven [b], E. Suard [c], J.L. Fourquet [b], F. Le Berre [b], M.P. Crosnier-Lopez [b,*]

[a] LEPMI BP75 1130 rue de la Piscine F-38402 Saint Martin d' Hères, France
[b] LdOF, FR n° 2575 IRIM2F, UMR CNRS 6010, Faculté des Sciences et Techniques, Université du Maine, Avenue O. Messiaen 72017 Le Mans Cedex 9, France
[c] Institut Laüe-Langevin, 6 rue G. Horowitz, 38042 Grenoble Cedex 9, France

ABSTRACT

The crystal structure of the Ruddlesden–Popper layered perovskite Li$_2$SrTa$_2$O$_7$ has been characterized at various temperatures between -185 and $300\,^\circ$C by several techniques: X-ray and neutron powder diffraction, single crystal diffraction, transmission electron microscopy and Raman spectroscopy. The low temperature structure has been confirmed to be orthorhombic *Cmcm* with a small octahedra antiphase tilting $(\Phi\Phi0)(\Phi\Phi0)$ inside the perovskite blocks. With temperature, the tilting progressively vanishes leading around $230\,^\circ$C to a tetragonal symmetry (S.G. *I4/mmm*). This reversible phase transition, followed by X-ray and neutron thermodiffraction and thermal Raman measurements, is considered as of second order. An attribution of the Raman bands based on normal mode analysis is proposed.

© 2008 Elsevier Inc. All rights reserved.

1. Introduction

Ruddlesden–Popper phases, with the general formula A$'_2$[A$_{n-1}$B$_n$O$_{3n+1}$], are of great interest for many of the properties they exhibit such as ion-exchange and intercalation [1], ionic conductivity [2], photocatalytic water splitting [3], giant magnetoresistance [4] and proton conduction [5] and exfoliation [6] on the protonated forms. The structure of these compounds can be described from that of perovskite: n BO$_6$ octahedra forming perovskite layers separated by A$'$ cations, A atoms occupying the perovskite cages (coordination number CN = 12). With this description, the limit $n = \infty$ represents the classical perovskite structure with an a_p cell parameter. In layered perovskites, tilting of the BO$_6$ octahedra is often observed in the perovskite blocks leading to a larger cell and a lower symmetry. The intensity of the superlattice reflections on the X-ray diffraction (XRD) powder patterns, arising from the octahedra tilts, are often too weak to be seen due to the low scattering factor of the O^{2-} anions compared to those of the A and B cations [7]. High-resolution powder neutron diffraction data are then essential to precisely determine the true cell as well as the position of light elements such as oxygen.

We determined a few years ago [8] the structure of Li$_2$SrTa$_2$O$_7$ from powder XRD data and found that it crystallizes in the *I4/mmm* space group (D_{4h}^{17}) with the following cell parameters: $a = 3.9499(2)$ and $c = 18.200(3)$ Å. This result, obtained with good reliability factors ($R_\mathrm{p} = 11.3\%$, $R_\mathrm{wp} = 12.0\%$, $R_\mathrm{exp} = 1.77\%$, $R_\mathrm{B} = 4.72\%$), were oddly in disagreement with the one simultaneously published by Floros et al. [9] (*Cmcm*, D_{2h}^{17}, $a = 18.189(1)$, $b = 5.5919(6)$ and $c = 5.5768(4)$ Å). According to their refined parameters, such an orthorhombic distorsion should have provided clear reflection splittings on the XRD pattern due to the symmetry lowering. Unfortunately, we did not see any splitting.

In order to clarify the disagreement between those two results, and after an optimization of the synthesis conditions, a complete structural study has been undertaken from neutron diffraction, Raman spectroscopy and Transmission Electron Microscopy (TEM). In addition, X-ray and neutron thermodiffraction and Raman measurements performed at various temperatures have both revealed a reversible phase transformation around $230\,^\circ$C. This transition, never observed until now for Li$_2$SrTa$_2$O$_7$, is also discussed in this paper.

2. Experimental

2.1. Preparation

In order to suppress the ambiguity concerning the crystallographic characteristics of Li$_2$SrTa$_2$O$_7$, very well crystallized

---

* Corresponding author. Fax: +33 2 43 83 35 06.
  E-mail address: marie-pierre.crosnier-lopez@univ-lemans.fr
(M.P. Crosnier-Lopez).

samples were needed. Such samples were obtained by solid state reaction in air from Ta_2O_5 (Alfa Aesar, 99.85%) and dry carbonates $^7Li_2CO_3$ (Euriso-Top, 99% ^7Li) and $SrCO_3$ (Aldrich, 99.9+%) in stoichiometric ratios with an excess of $^7Li_2CO_3$ (10% mol) to compensate for the oxide volatility at high temperature. ^7Li was used to reduce the absorption cross-section in neutron diffraction experiments. The reagents were ground in an agate mortar, pressed into pellets and placed on a platinum sheet. The pellets
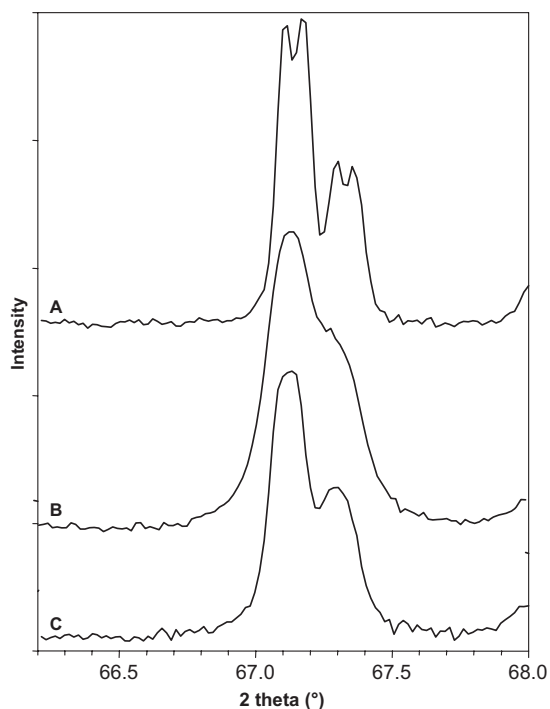
were pre-heated at 550 °C for 6 h to decompose carbonates and then heated at 1150 °C for 6 h. After grinding, pellets were heated again at 1150 °C for 20 h with another intermediate grinding. A final heating was then performed in a sealed platinum tube at 1300 °C for 15 h, followed by a cooling at 25 °C/h to room temperature. Fig. 1 shows a selected part of the XRD pattern corresponding to this sample named A. For comparison, we have added the same selected part of the XRD pattern for a sample obtained from the procedure described by Floros et al. [9] (sample B) and for one corresponding to the synthesis detailed in our previous paper [8] (sample C). This figure confirms that we improved the crystallinity. Consequently, all the following structural results concern the A sample.

2.2. Powder diffraction data

The powder XRD patterns were recorded in air with a PANalytical X'pert Pro diffractometer equipped with the X'Celerator detector using $CuK\alpha$ radiation. For thermal measurements (TXRD), the diffractometer was equipped with an Anton Paar HTK 12 furnace. A delay of 5 min was systematically applied before recording diffraction patterns (heating rate 5 °C/min). For the room temperature experiment (RT), the data were collected in the 5.00–130.00° 2θ range with a 0.017° step scan increment and 250 s time/step. For the thermal measurements, the data range collection was 8.00–120.00° 2θ with a 0.017° step scan increment and 210 s time/step.

The neutron powder diffraction patterns were recorded at ILL on D2B high-resolution neutron diffractometer (easy access fast sampling for RT). The experimental conditions are: $\lambda = 1.59484(1)$ Å, angular range (deg 2θ) = 0.10–158.70, step scan increment (deg 2θ) = 0.05, counting time = 4 h for RT measurement, and at 300 °C, $\lambda = 1.59455(1)$ Å, angular range (deg 2θ) = 0.10–159.95, step scan increment (deg 2θ) = 0.05, counting time = 5 h.

For all the diffraction data, the structure refinements were carried out by the Rietveld method using the Fullprof refinement
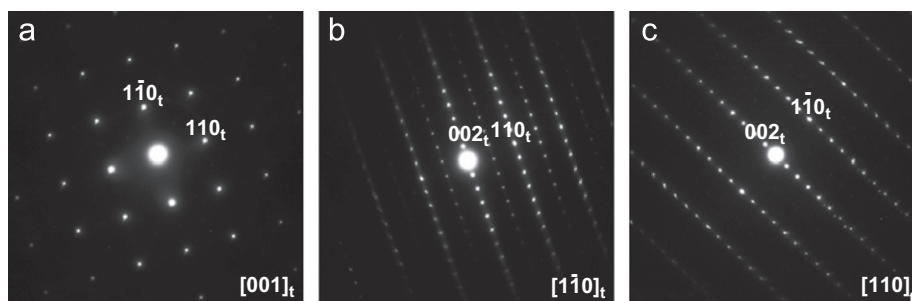

Fig. 1. Selected part of XRD patterns showing a line splitting for A, B and C samples.

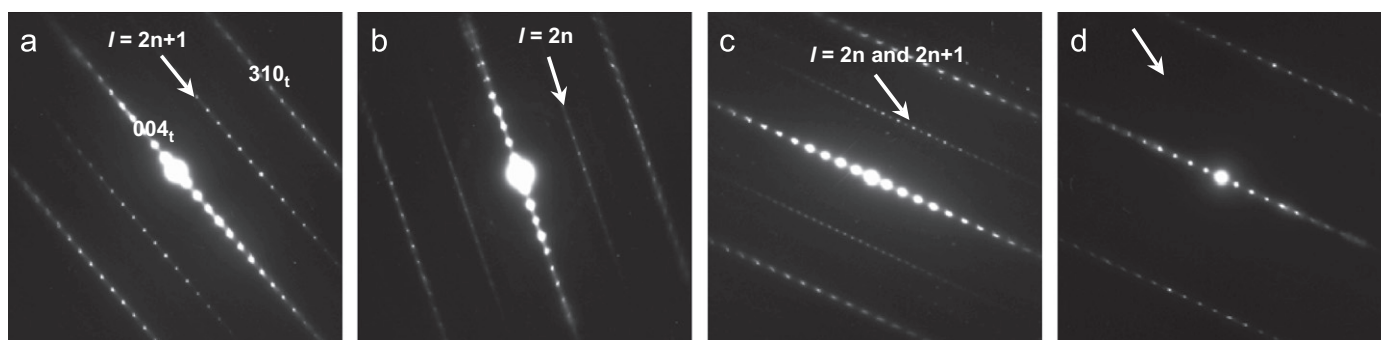**Fig. 2.** Typical SAED patterns of $Li_2SrTa_2O_7$ along three zone axis.

Fig. 3. SAED patterns of $Li_2SrTa_2O_7$ showing twinning and defects (see text).
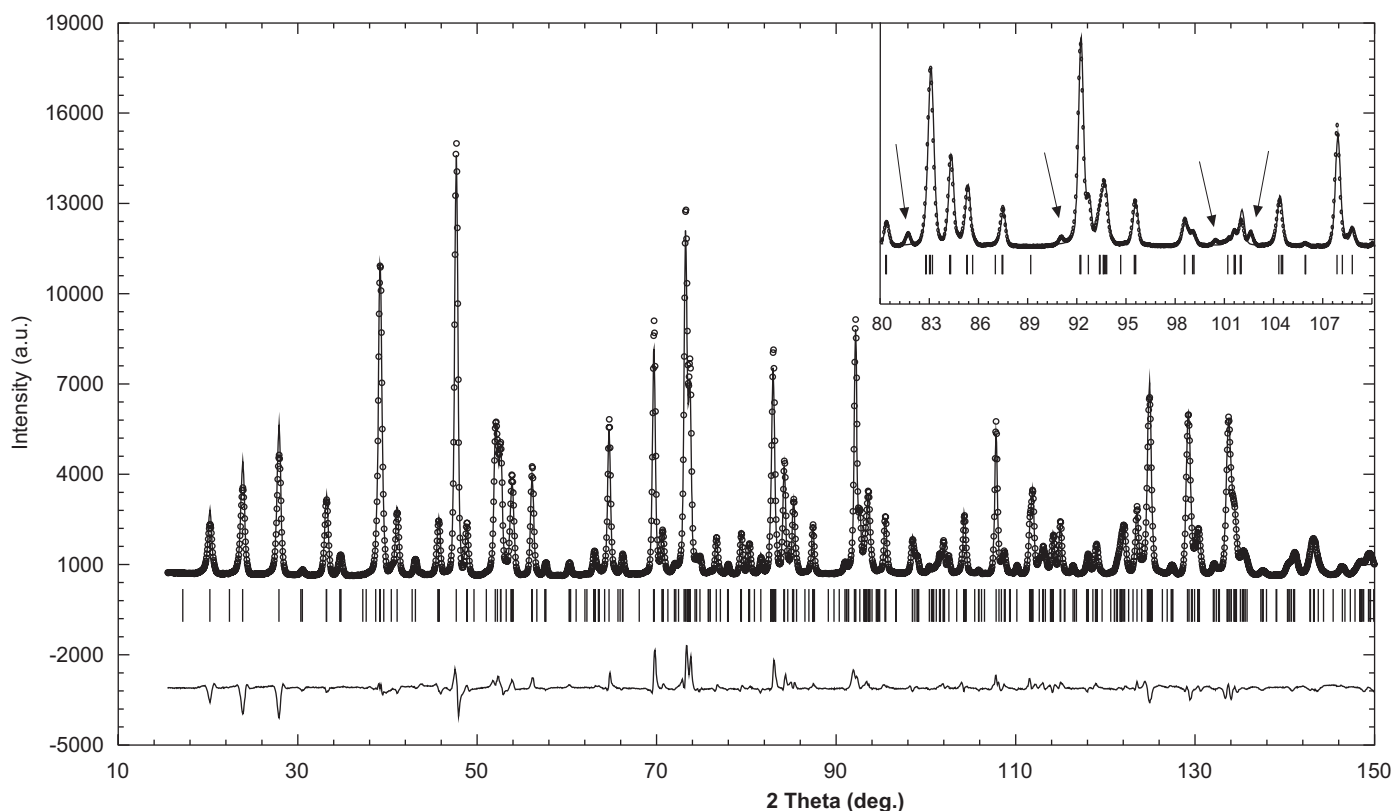
Fig. 4. Observed, calculated and difference neutron patterns of $Li_2SrTa_2O_7$ at RT in the *Cmcm* space group. Vertical bars are related to the calculated Bragg reflection positions. The inserted zoom shows lines not indexed in *Fmmm* space group.

Table 1
Structure refinement results of $Li_2SrTa_2O_7$ from neutron data.

	Neutrons	
	RT	300 °C
Space group	*Cmcm*	*I4/mmm*
Number of refined parameters	43	39
Peak shape, η	Pseudo-Voigt	Pseudo-Voigt
	0.40(2)	0.09(2)
Cell parameters/Å	$a = 18.1822(3)$	$a = 3.9531(1)$
	$b = 5.5844(2)$	
	$c = 5.5797(2)$	$c = 18.3102(2)$
Halfwidth parameters	$u = 0.156(3)$	$u = 0.060(1)$
	$v = -0.360(7)$	$v = -0.150(3)$
	$w = 0.313(4)$	$w = 0.153(2)$
	$x = 0.0004(3)$	$x = 0.0030(3)$
Asymmetry parameters	$P_1 = 0.038(6)$	$P_1 = 0.048(7)$
	$P_2 = 0.019(3)$	$P_2 = 0.024(3)$
R_{Bragg}	5.46%	5.21%
R_p	9.61%	10.9%
R_{wp}	11.10%	11.6%
R_{exp}	1.43%	2.86%
χ^2	59.90	16.40

Table 2
Atomic coordinates, B_{iso} and bond valence sums ($\sum$) for $Li_2SrTa_2O_7$ from neutron diffraction data at RT (S.G.: *Cmcm*).

	Site	s.o.f.	x	y	z	B (10^{-2} Å^2)	$\sum$ ($\sum_{exp}$)
Ta	8g	1	0.11448(8)	0.7530(6)	0.25	0.56(2)	5.1 (5)
Sr	4c	1	0	0.2553(9)	0.25	0.86(3)	2.2 (2)
O1	8e	1	0.6117(1)	0	0	1.11(4)	2.0 (2)
O'1	8e	1	0.0968(1)	0	0	0.72(4)	2.1 (2)
O2	8g	1	0.2176(1)	0.7701(7)	0.25	0.80(4)	1.9 (2)
O3	4c	1	0	0.7187(9)	0.25	0.91(6)	2.0 (2)
Li	8e	1	0.2579(4)	0	0	0.76(7)	0.8 (1)

program [10]. For each pattern, a pseudo-Voigt function was chosen to generate the line shape of the diffraction peaks and the background level was first defined manually before being refined. In addition to the atomic and thermal parameters, the scale factor, the zero point and the cell parameters were refined.

2.3. Single crystal diffraction data

A small crystal of approximate volume 1.2×10^{-4} mm^3 with natural boundary faces $\langle 210 \rangle$, $\langle -110 \rangle$ and $\pm \langle 001 \rangle$, $\langle 110 \rangle$ was

selected for the X-ray data collection on a Siemens AED2 four circle diffractometer (radiation MoKα graphite monochromatized). The registered range was: $2\theta_{max} = 70.07°$ with $-4 \leqslant h \leqslant 4$, $-6 \leqslant k \leqslant 6$ and $-28 \leqslant l \leqslant 29$.

2.4. TEM study

For TEM study, the sample was prepared as follows: a small amount of powder was ultrasonically dispersed in absolute ethanol and one droplet of this suspension was deposited onto a carbon film supported on a copper grid. The microscope used for this study was a JEOL 2010 (200 kV) equipped with a side-entry $\pm 30°$ double tilt specimen holder.

2.5. Raman

Raman spectra were collected with a Jobin-Yvon T64000 spectrometer in triple subtractive configuration. The exciting line was the 488 nm line of an Ar laser. All experiments were carried

out on powders in micro-Raman configuration, with a laser power of about 5 mW on the sample. Thermal measurements were carried out with a laboratory made cell. Spectra decomposition in individual Lorentzian bands was carried out with a laboratory made program based on simulated annealing [11].

3. Results

3.1. Room temperature

With the synthesis conditions described in Refs. [8,9] no split due to an orthorhombic distortion can be observed on the XRD pattern of samples B and C and a good fit can be obtained within the $I4/mmm$ space group.

For sample A, a small splitting of some lines is immediately evidenced: this splitting is characteristic of the departure from tetragonal symmetry. An orthorhombic supercell ($Fmmm$ space group) with $a \approx \sqrt{2}a_p$, $b \approx \sqrt{2}a_p$ and $c \approx 18.2$ Å allows for a good indexation of the whole pattern. Starting from the $BaNd_2Mn_2O_7$ perovskite slabs structural model [12] and with strontium located in a 8 g site (x, 0, 0) with a half-occupancy factor, the refinements converged quickly to very good reliability factors ($R_p = 10.70\%$, $R_{wp} = 9.45\%$ and $R_{Bragg} = 3.58\%$). All the refined parameters are given as supplementary data as well as the obtained calculated pattern.

As in this $Fmmm$ space group, no octahedra tilt is considered, we performed single crystal XRD which is much more sensitive to octahedra tilts in RP phases [7,13]. We therefore selected one small colorless single crystal (1.2×10^{-4} mm³). However, no supercell was found and the refinement could be carried out satisfactorily in the $I4/mmm$ space group with very good reliability factors: $R = 0.0176$ for 219 data with $Fo > 4\sigma(Fo)$ and 0.0182 for all 222 data with maxima and minima of the final Fourier difference synthesis about ± 2.2 e⁻/Å³. Taking into account the low value of the temperature phase transition, we can think

Table 3
Selected interatomic distances (Å) for $Li_2SrTa_2O_7$ at RT and 300 °C from neutron diffraction data.

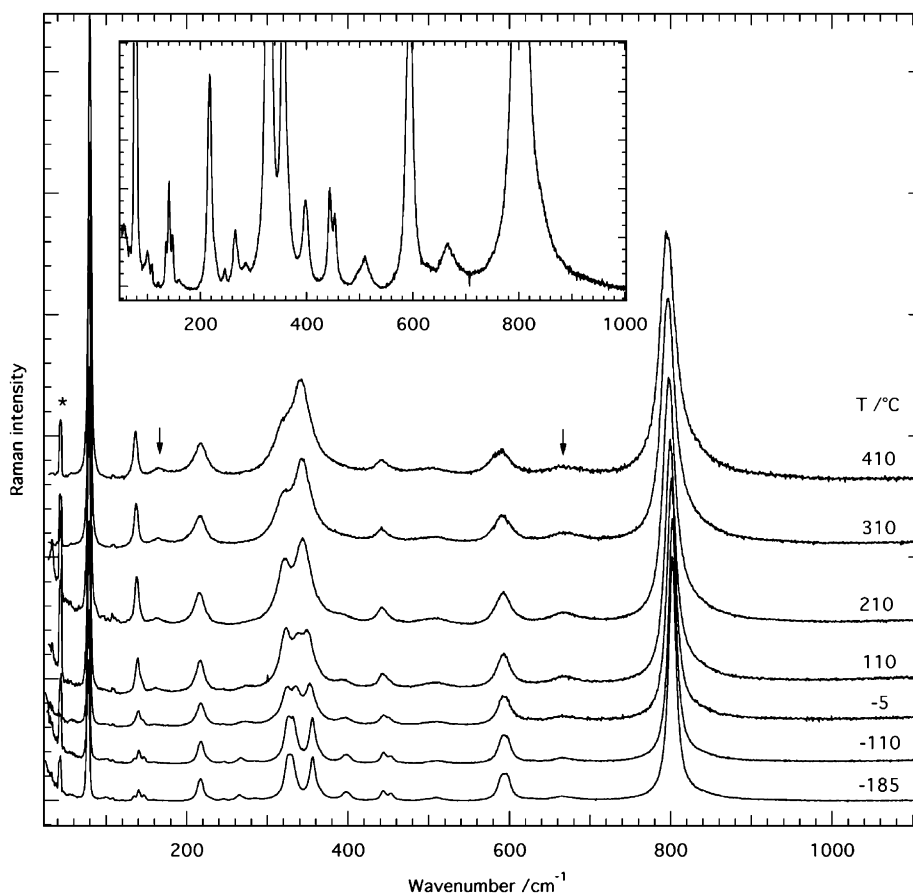| Ta octahedra		Sr polyhedra		Li tetrahedra	
RT	300 °C	RT	300 °C	RT	300 °C
Ta–O1: 2 × 1.9859(3)	Ta–O1: 4 × 1.9843(5)	Sr–O1: 4 × 2.8175(2)	Sr–O1: 8 × 2.7509(4)	Li–O2: 2 × 2.0320(2)	Li–O2: 4 × 2.0678(5)
Ta–O'1: 2 × 1.9880(2)	Ta–O2: 1 × 1.8812(1)	Sr–O'1: 4 × 2.6604(2)	Sr–O3: 4 × 2.7953(5)	Li–O2: 2 × 2.1023(3)	
Ta–O2: 1 × 1.8779(1)	Ta–O3: 1 × 2.0888(1)	Sr–O3: 1 × 2.5875(5)			
Ta–O3: 1 × 2.0903(1)		Sr–O3: 2 × 2.7936(5)			
		Sr–O3: 1 × 2.9969(5)			

Fig. 5. Raman spectra of $Li_2SrTa_2O_7$ at various temperatures. The star indicates a spurious line, and the arrows second order bands. Insert: expanded view of the spectrum taken at −185 °C showing the small bands due to $Cmcm$ distortion.

that all the crystallites are not exactly in the same equilibrium state despite the synthesis conditions applied (very slow cooling rate). All the other single crystals tested were unfortunately twinned and did not provide any interesting information.

At this stage, a TEM study was undertaken and it revealed first that all particles were thin and well crystallized. Typical SAED patterns (Fig. 2) are indexed according to the ideal tetragonal $I4/mmm$ structure (t) ($a_p \approx 3.9$ and $c \approx 18.2$ Å), but additional weak reflections imply a larger cell: $a \approx \sqrt{2}a_p$, $b \approx \sqrt{2}a_p$, c. In this supercell, extinction conditions are inconsistent with the $Fmmm$ orthorhombic space group, but in good agreement with $Cmcm$ proposed by Floros et al. [9]. However, as usually encountered for orthorhombic phases with two very close parameters, twinning phenomena are often observed as shown in Fig. 3, corresponding to the same $[\overline{1}30]_t$ zone axis. Pattern (c) is obtained by the superposition of the two patterns (a) and (b) corresponding at least to two domains with a and b parameters exchanged. On pattern (d), no additional reflection can be seen meaning that no tilt of the octahedra inside the perovskite layer is observed for that crystallite: the ideal tetragonal cell ($a_p \approx 3.9$ and $c \approx 18.2$ Å $I4/mmm$) is then sufficient to describe its structure, as observed for the single crystal studied by XRD. Moreover, on pattern (b), diffuse streaks can be observed due to stacking defects along the c direction and/or to intergrowth with other n members RP phase.

Since no evidence of octahedra tilts can be detected on the XRD pattern, neutron diffraction patterns were recorded. We quickly observed that some lines of this pattern could not be indexed in the $Fmmm$ space group (Fig. 4—zoom part), while they were

perfectly indexed in the space group $Cmcm$ (Fig. 4) and the acentric corresponding one $Cmc2_1$. For the refinements, the starting fractional coordinates of each site were taken from that of $Li_2SrNb_2O_7$ [9] and the final reliability factors were satisfactory (Table 1) although the χ^2 factor remains very high. The atomic coordinates obtained from the neutron diffraction data are given in Table 2 while interatomic distances and bond valence sums using the Zachariasen law [14] are in Tables 3 and 2, respectively.

Raman spectroscopy can be very useful in the structure determination of oxides, because the number of observed bands is strongly dependent on symmetry. For the three possible space groups, using the atomic positions determined previously, the mechanical representations are

for $I4/mmm$ $3A_{1g}(R) + 2B_{1g}(R) + 5E_g(R) + 6A_{2u}(IR) + B_{2u}(s) + 7E_u(IR)$;

for $Fmmm$ $4A_g(R) + 3B_{1g}(R) + 6B_{2g}(R) + 5B_{3g}(R)$
$+ A_u(S) + 6B_{1u}(IR) + 6B_{2u}(IR) + 6B_{3u}(IR)$;

for $Cmcm$ $9A_g(R) + 12B_{1g}(R) + 8B_{2g}(R) + 7B_{3g}(R)$
$+ 5A_u(s) + 10B_{1u}(IR) + 12B_{2u}(IR) + 9B_{3u}(IR)$.

Ten bands are thus expected in the $I4/mmm$ structure, 18 in the $Fmmm$ structure, and 36 in the $Cmcm$ structure. Raman spectra obtained at RT or below show, after decomposition into individual Lorentzian elements, 28 bands (Fig. 5 and Table 4). The low temperature structure is thus likely to be $Cmcm$.

3.2. Thermal study

An X-ray thermodiffraction study was undertaken. Fig. 6 shows the transformation with temperature of two selected lines of the XRD pattern. When the temperature rises, the diffraction lines

Table 4
Raman bands characteristic at 410 and −185 °C, and attributions.

$I4/mmm$ (410 °C)			$Cmcm$ (−185 °C)			Attribution
Pos	Width	Rel ampl	Pos	Width	Rel ampl	
79.0	3.15	100	76.8	2.48	41	Ta Ty, Tz
80.7	2.70	90.5	78.4	2.55	50	S_{17}, S_{18}
			100.0	6.39	1.3	
			108.2	4.11	0.8	
			121.0	2.49	0.3	
			134.8	4.57	1.9	
136.4	5.90	14.8	140.6	3.58	5.1	Ta, Tx S_1
			147.1	4.20	2.4	
165.0	14.89	1.9	160.15	5.07	0.1	2nd order
217.2	18.39	9.8	217.1	8.63	10.8	S_{11}
			228.8	6.07	0.5	
			245.9	3.49	0.9	
			265.5	9.53	2.6	
			284.2	13.89	0.5	
317.9	23.90	9.5	325.1	9.73	14.6	S_{10}
			331.2	10.33	15.0	S_{19}, S_{20}
341.6	29.49	27.5	356.1	8.72	19.7	S_{25}, S_{26}
			366.6	9.85	1.5	
			397.9	12.66	3.8	
442.3	20.09	3.8	443.6	7.08	4.4	S_3
			453.1	7.60	2.9	
			497.4	10.82	0.4	
499.0	48.99	1.7	509.3	12.84	1.4	
			520.2	10.18	0.5	
587.8	26.96	8.3	589.4	11.12	9.3	Ta–O1 asym stretch
			596.6	10.92	9.0	S_{21}, S_{22}
			627.3	9.34	0.4	
666.8	35.41	2.0	665.2	25.13	1.6	2nd order
795.9	22.13	72.6	802.07	10.91	100	Ta–O2 stretch S_2

Symmetry coordinates labels refer to Table 7.
Degenerate modes in the high temperature phase are isolated by horizontal lines.
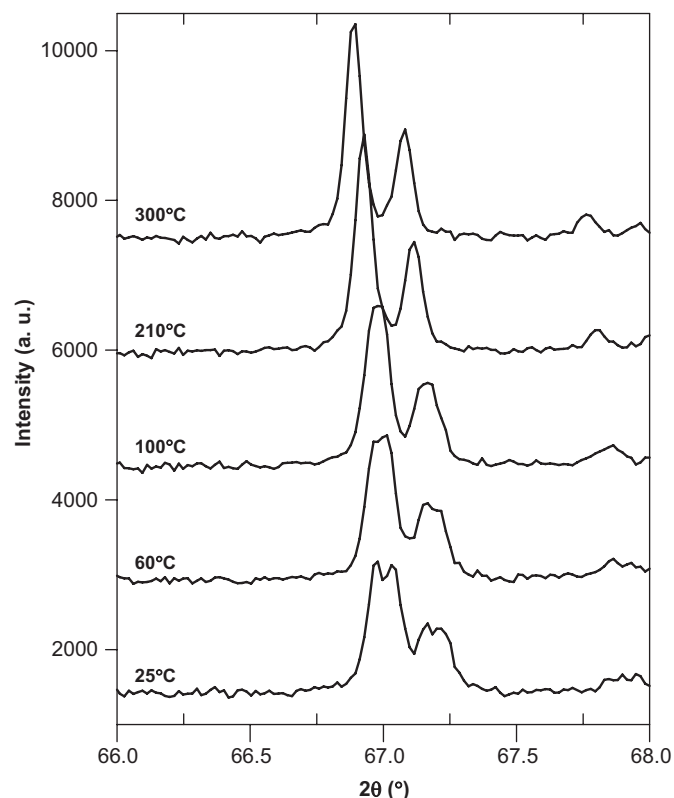

Fig. 6. Thermal evolution of $Li_2SrTa_2O_7$ X-ray powder diffraction patterns between 25 and 300 °C showing the structural transformation from orthorhombic to tetragonal cell.

splitting decreases, implying a progressive vanishing of the orthorhombic distortion. The evolution of unit cell parameters versus temperature are given in Fig. 7: the cell parameters increase continuously and above 300 °C, the a and b parameters equalize. At 300 °C, a complete structural refinement was performed in the $I4/mmm$ space group from neutron data. It led to good reliability factors (Table 1) and to a good agreement between the observed and calculated patterns (Fig. 8). Table 5 gathers the atomic coordinates, while interatomic distances and bond valence sums using the Zachariasen law [14] are given, respectively, in Tables 3 and 5.

This reversible structural phase transition can be also observed during HREM imaging, since the $h\,k\,l$ reflections leading to the supercell $\sqrt{2}a_p$ disappear while the spots corresponding to the $I4/mmm$ space group remain, in good agreement with the diffraction results obtained at 300 °C.

In parallel to this thermodiffraction study, thermal RAMAN experiments were undertaken. The spectra obtained at various temperatures are shown in Fig. 5. The most intense bands which are observed at low temperature are still present in the whole temperature range. Above 200 °C, some bands merge and bands with a small intensity disappear (Fig. 9). This is more visible in Fig. 10 for medium and low intensity bands. Two broad bands signaled by an arrow in Fig. 5 show a marked increase in their intensi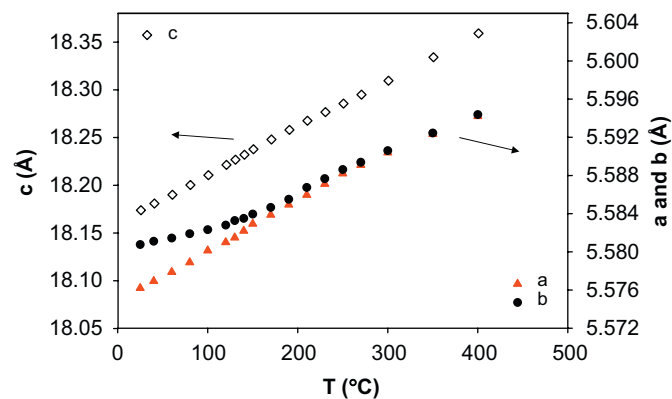ty when temperature increases and can be assigned to second order bands. Table 4 gives the characteristics of the Lorentzian bands at low and high temperatures. Most of the bands soften when temperature increases. That is consistent with the positive thermal expansion confirmed by TXRD data. Some bands, however, strengthen: the two bands near 80 cm^{-1}, the band at 265 cm^{-1}, and the band at 330–340 cm^{-1}, which shifts from the band at 320 cm^{-1} (at −185 °C) to the band at 350 cm^{-1} and finally merge with it at 200 °C.

4. Discussion

4.1. Crystallographic structure and phase transition

The crystallographic structure of a well crystallized sample Li$_2$SrTa$_2$O$_7$ (sample A) at RT is confirmed to be $Cmcm$, as proposed by Floros et al. [9], but the departure from tetragonal structure is, however, less pronounced (4.7 10^{-3} Å from neutron data, instead of their published value 15.1 × 10^{-3} Å). From a crystallographic point of view, the transformation from $I4/mmm$ space group to the standard orthorhombic $Cmcm$ space group is characterized by a cell volume doubling with the following axes permutation:

$$\begin{cases} \vec{a}_O = \vec{c}_T \\ \vec{b}_O = \vec{a}_T - \vec{b}_T \\ \vec{c}_O = \vec{a}_T + \vec{b}_T \end{cases}$$

where the o index refers to the orthorhombic cell and the T to the tetragonal one. The tetragonal to orthorhombic transition ($I4/mmm \rightarrow Cmcm$) is characterized by a rotation of TaO$_6$ octahedra

Fig. 7. Evolution of the unit cell parameters versus temperature for Li$_2$SrTa$_2$O$_7$.

Table 5
Atomic coordinates, B_{iso} and bond valence sums ($\sum$) for Li$_2$SrTa$_2$O$_7$ from neutron diffraction data at 300 °C (S.G.: $I4/mmm$).

	Site	s.o.f.	x	y	z	B (10^{-2} Å^2)	Σ (Σ_{exp})
Ta	4e	1	0	0	0.38592(7)	0.41(2)	5.1 (5)
Sr	2a	1	0	0	0	1.32(4)	2.1 (2)
O1	8g	1	0	0.5	0.1045(1)	1.13(3)	2.1 (2)
O2	4e	1	0	0	0.2832(1)	1.29(4)	1.9 (2)
O3	2b	1	0	0	0.5	1.57(5)	1.9 (2)
Li	4d	1	0	0.5	0.25	1.97(9)	0.8 (1)

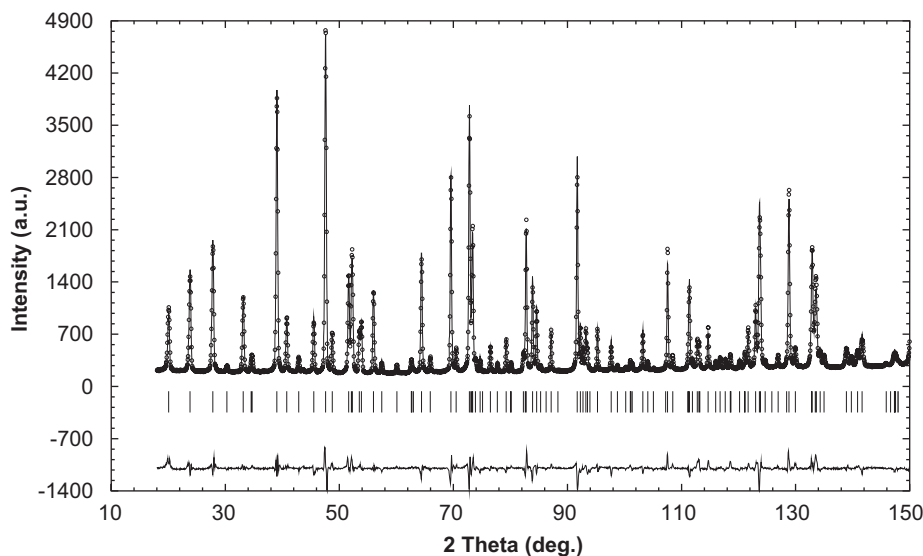
Fig. 8. Observed, calculated and difference neutron diffraction patterns of Li$_2$SrTa$_2$O$_7$ at 300 °C in the $I4/mmm$ space group. Vertical bars are related to the calculated Bragg reflection positions.

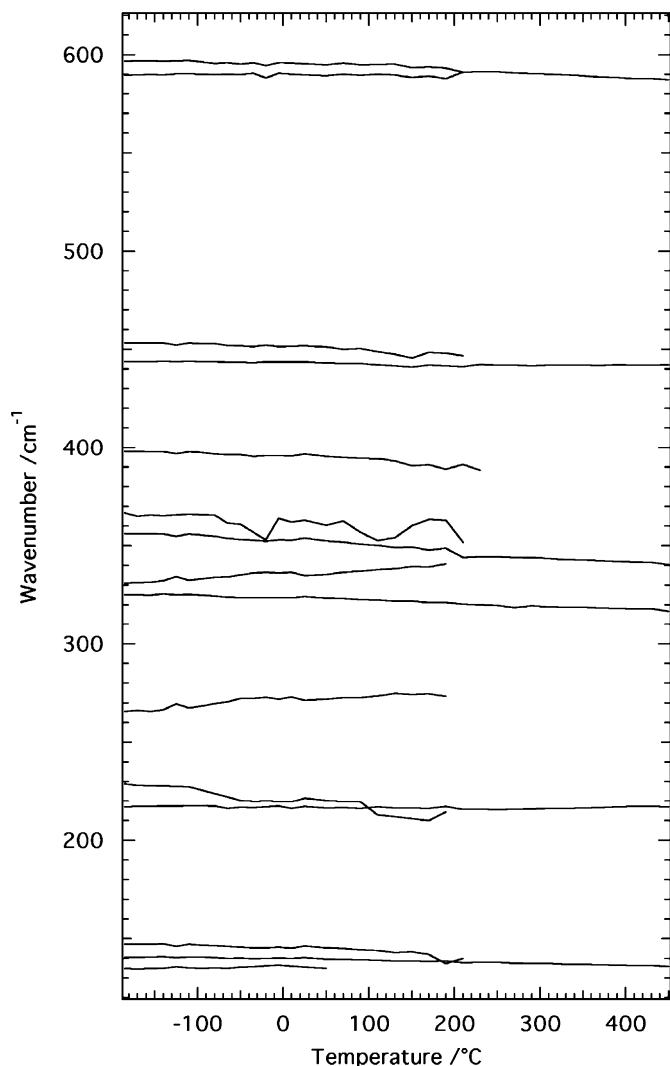**Fig. 9.** Changes in major Raman band wavenumbers as a function of temperature. Note the strong variations in the 210–230 °C region.

Fig. 10. Detailed view of the middle wavenumber part of the Raman spectra. Only some temperatures are indicated.

inside the perovskite layers which can be written $(\Phi\Phi0)$ $(\Phi\Phi0)$ according to the standard symbolism proposed by Aleksandrov et al. [15]. This scheme means that there is an equal antiphase tilt Φ simultaneously along the a and b axis of the aristotype $I4/mmm$ space group and that two adjacent slabs are identical.

Since the distortion from tetragonal structure involves mainly light atoms (Li and O), XRD is generally not sufficient to determine the exact structure. This is clearly shown once more in the case of $Li_2SrTa_2O_7$ for which a very realistic structure can be proposed in the orthorhombic space group $Fmmm$ showing no octahedra tilting inside the perovskite layers (see the supplementary data). The small octahedral tilt, about 3.9° in the $Cmcm$ space group (Fig. 11) compared to their straight position in $Fmmm$, is only depicted from neutron diffraction experiments. The resulting interatomic distances (Table 3) and the bond valence sums (Table 2) are very close to those obtained in the $Fmmm$ model from XRD data (see the supplementary data). The Li atoms are located between the perovskite layers in a distorted tetrahedral coordination with Li–O distances equal to 2.0320(2) and 2.1023(3) Å. Even if it is not strictly a structure determination method, Raman spectroscopy is useful to distinguish between various possibilities. The result is here particularly clear. From the
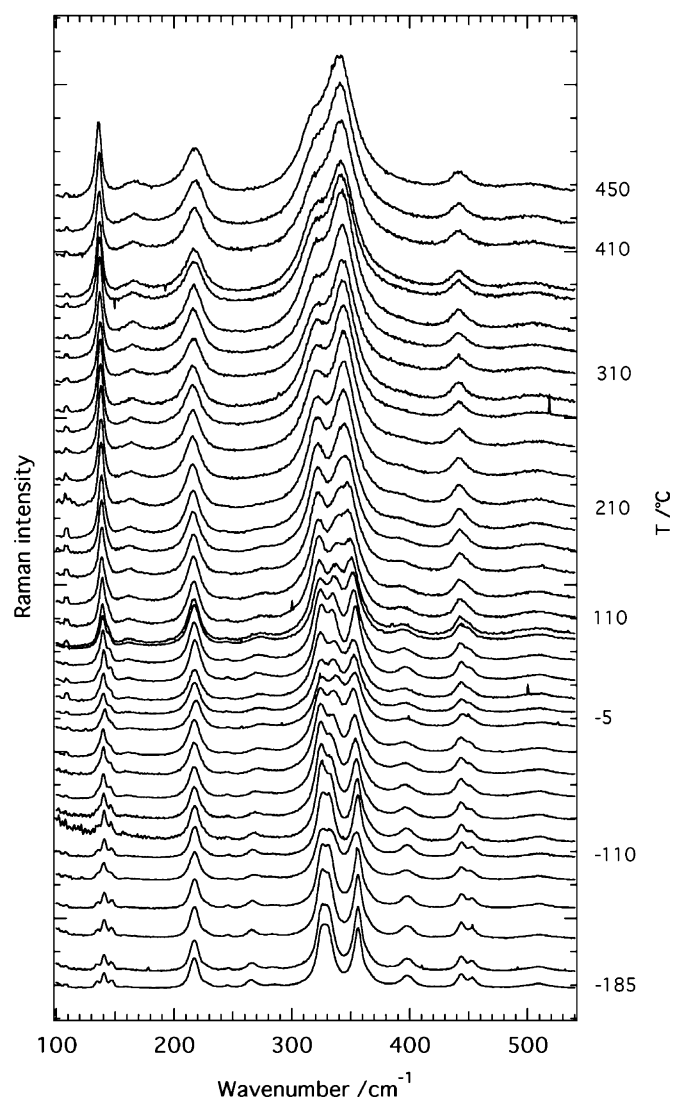
possible structures, only $Cmcm$ is consistent with Raman data at low temperature.

However, the TEM study and the monocristal diffraction experiment have clearly revealed that the compound $Li_2SrTa_2O_7$ presents defects at RT. Indeed, the rotation of the TaO_6 octahedra is not always observed since the structure of some crystallites could be described in the $I4/mmm$ space group with straightened up octahedra inside the perovskite layers. In such conditions, we think that the $Cmcm$ structure corresponds to the well organized phase, a situation which is more or less reached in the crystallites depending on the synthesis conditions. One cannot exclude that the octahedral units rotation can be different from one crystallite to another one or inside a same crystallite, as discussed for the layered perovskite $Sr_3Ir_2O_7$ [16,17].

Raman spectra and thermal diffraction indicate both that a phase transition occurs near 230–240 °C towards a more symmetric structure: in the RAMAN spectra, bands disappear between 210 and 230 °C. The transition temperature can thus be estimated at 230±20 °C. The $I4/mmm$ space group is therefore proposed for the high temperature phase.

The evolutions of the wavenumbers of various bands in the transition temperature region are continuous and smooth. This suggests a second order transition. Table 6 gives the correspondence between atomic positions in both phases.
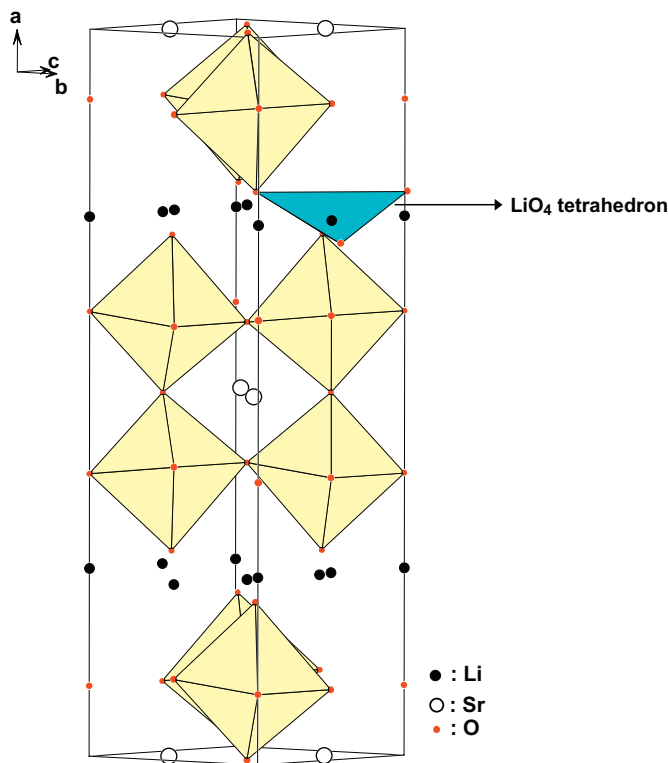
Fig. 11. Projection of the structure of $Li_2SrTa_2O_7$ in the low temperature form (*Cmcm*), showing the small octahedra tilting.

Table 6
Atomic positions in the two forms of $Li_2SrTa_2O_7$.

Positions in *I4/mmm*	Positions in *Cmcm*	
Li_1 (1/4, 0, 1/2)	Li_4 (0.26, 0, 1/2)	Li_3 (0.24, 1/2, 0)
Li_2 (1/4, 0, 0)	Li_1 (0.26, 0, 0)	Li_2 (0.24, 1/2, 1/2)
Sr (0, 1/4, 1/4)	Sr_1 (0, 0.26, 1/4)	Sr_2 (0, 0.74, 3/4)
Ta_1 (0.38, 1/4, 1/4)	Ta_3 (0.39, 0.25, 1/4)	Ta_2 (0.39, 0.75, 3/4)
Ta_2 (0.62, 1/4, 1/4)	Ta_1 (0.61, 0.25, 1/4)	Ta_4 (0.61, 0.75, 3/4)
$O1_1$ (0.60, 0, 0)	$O1_1$ (0.61, 0, 0)	$O'1_4$ (0.60, 1/2, 1/2)
$O1_2$ (0.60, 0, 1/2)	$O1_4$ (0.61, 0, 1/2)	$O'1_1$ (0.60, 1/2, 0)
$O1_3$ (0.40, 0, 0)	$O1_3$ (0.39, 0, 0)	$O'1_2$ (0.40, 1/2, 1/2)
$O1_4$ (0.40, 0, 1/2)	$O1_2$ (0.39, 0, 1/2)	$O'1_3$ (0.40, 1/2, 0)
$O2_1$ (0.28, 1/4, 1/4)	$O2_3$ (0.28, 0.27, 1/4)	$O2_2$ (0.28, 0.73, 3/4)
$O2_2$ (0.72, 1/4, 1/4)	$O2_1$ (0.72, 0.27, 1/4)	$O2_4$ (0.72, 0.73, 3/4)
$O3$ (1/2, 1/4, 1/4)	$O3_1$ (1/2, 0.22, 1/4)	$O3_2$ (1/2, 0.78, 3/4)

Fractional coordinates are of the orthorhombic axes.
Fractions (or 0) values indicate a special position along the corresponding axis.

At 300 °C and from neutron data, the refined structure of $Li_2SrTa_2O_7$ in the *I4/mmm* space group presents straightened perovskite layers with Ta–O distances close to those observed at RT (Table 3), the four equatorial distances Ta–O1 and Ta–O′1 being equal. The slightly c parameter increase between RT and 300 °C (18.1822–18.3102 Å) results mainly in an increase of the interlayer spacing (1.177–1.215 Å) with constant Li–O distances ($\langle$Li-O$\rangle$ = 2.067 Å at RT compared to Li–O = 2.068 Å at 300 °C) and octahedra heights (3.967 Å at RT and 3.970 Å at 300 °C).

Differential thermal analysis shows no peak in this temperature range, confirming the second order nature of the phase transition.

4.2. Raman bands attribution

Table 7 gives the symmetry coordinates for the two structures. Displacements along the $c_T(a_O)$ axis are bases of A_{1g} and B_{1g} vibrations, while displacements in the (a_T, b_T) plane are bases of the E_g modes in *I4/mmm*. There are close relations between symmetry coordinates in both phases, and they have been written in Table 7 to show them. A_{1g} vibrations in the high symmetry phase transform into A_g vibrations in the low symmetry one. B_{1g} transform into B_{3g} while E_g transform into one B_{1g} and one B_{2g} vibrations.

The attribution of some of the bands allowed in the tetragonal structure is rather straightforward. The short Ta–O2 bond stretching (coordinate S_2 in Table 7) must appear at the highest frequency. Then must appear the Ta–O1 bond stretching frequencies, corresponding to symmetry coordinates S_{21} and S_{22}. This vibration is degenerate in the tetragonal structure. On the opposite part of the spectrum, the lowest wavenumber bands must correspond to Ta displacements. Displacements along a_O (coordinate S_1) are of symmetry A_{1g}, while displacements in the (b_O, c_O) plane (S_{17} and S_{18}) are degenerate in the tetragonal structure. One would attribute the band at 136.4 cm^{-1} to S_1 and the doublet observed at low temperature at 76.8 and 77.4 cm^{-1} to S_{17} and S_{18}. However, it is always better to decompose this last band into two components, even when only one E_g band is expected at high temperature. The apparent width of the band, taken graphically on the spectra, shows first a decrease and then an increase (Fig. 12). Such changes are consistent with the progressive merge of two bands (the apparent width decreases) followed by thermal enlargement when the two bands have merged. We therefore attribute the bands near 80 cm^{-1} to the E_g mode in the high temperature phase and to the $B_{1g}+B_{2g}$ modes in the low temperature phase, and the 136.4 cm^{-1} band to S_1. This attribution is also consistent with the fact that the Ta displacements along the a_O axis imply to some extent the strong Ta–O2 bond, and must therefore be at higher frequency than the perpendicular displacements.

The other modes of the tetragonal structure can be attributed using previous attributions for similar layered titanates [18,19]. There is one band at 442 cm^{-1} in the high temperature spectra and two bands at 443 and 453 cm^{-1} at low temperature. One could therefore attribute it to an E_g mode in the *I4/mmm* structure. However, the high wavenumber component appears first as a shoulder of the stronger 442 cm^{-1} component just below the transition temperature. We thus prefer to attribute the band at 442 cm^{-1} to a non-degenerate mode corresponding to symmetry coordinate S_3, which is very close to the v_4 vibration of the octahedron. The v_4 vibration appeared near 380 cm^{-1} in various titanates [18]. In the region 300–420 cm^{-1}, there are at least two bands at high temperature and three at low temperature. In each phase, these bands must belong to different symmetries otherwise mode interaction should split them into well separated bands [20]. At high temperature, the band at 341.6 cm^{-1} must be of E_g symmetry, while the band at 317.9 cm^{-1} must be non-degenerate. In sodium titanates, bands of this spectral domain have been attributed to $(NaO)_2$ vibrations [19]. In $Li_2SrTa_2O_7$, vibrations along the x axis of Li and O2 are fully decoupled, because they do not belong to the same symmetry. We therefore attribute the band at 317.9 cm^{-1} to the symmetry coordinate S_{10}. For vibrations in the (y,z) plane, vibrations of Li and O2 can couple. The band at 341.6 cm^{-1} can therefore be attributed to a mixture of S_{25} and S_{26} (for lithium), and S_{19} and S_{20} (for O2 atoms). All visible bands of the high temperature structure have been thus identified. Two E_g modes are missing. One is the second combination of symmetry coordinates S_{19}, S_{20}, S_{25}, and S_{26}. It could lie in the region 250–350 cm^{-1} and be of low intensity. The other one corresponds to symmetry coordinates S_{23} and S_{24} and is a pure Ta–O1 bending mode. At high temperature, it could be hidden by the A_{1g} mode at 136 cm^{-1} and be at the origin of the two very similar modes observed at 135 and 147 cm^{-1} at low temperature.

Table 7
Symmetry coordinates in the low and high temperature forms of $Li_2SrTa_2O_7$.

| Name	$I4/mmm$ structure	$Cmcm$ structure
	A_{1g}	**A_g**
S_1	xTa_1-xTa_2	$xTa_1-xTa_2-xTa_3+xTa_4$
S_2	$xO2_1-xO2_2$	$xO2_1-xO2_2-xO2_3+xO2_4$
S_3	$xO1_1+xO1_2-xO1_3-xO1_4$	$(xO1_1-xO1_2-xO1_3+xO1_4)+(xO'1_1-xO'1_2-xO'1_3+xO'1_4)$
S_4		$(xO1_1-xO1_2-xO1_3+xO1_4)-(xO'1_1-xO'1_2-xO'1_3+xO'1_4)$
S_5		$xLi_1-xLi_2-xLi_3+xLi_4$
S_6		$yTa_1-yTa_2+yTa_3-yTa_4$
S_7		$yO2_1-yO2_2+yO2_3-yO2_4$
S_8		$yO3_1-yO3_2$
S_9		xSr_1-xSr_2
	B_{1g}	**B_{3g}**
S_{10}	xLi_1-xLi_2	$xLi_1+xLi_2-xLi_3-xLi_4$
S_{11}	$xO1_1-xO1_2-xO1_3+xO1_4$	$(xO1_1+xO1_2-xO1_3-xO1_4)-(xO'1_1+xO'1_2-xO'1_3-xO'1_4)$
S_{12}		$(xO1_1+xO1_2-xO1_3-xO1_4)+(xO'1_1+xO'1_2-xO'1_3-xO'1_4)$
S_{13}		$zTa_1-zTa_2+zTa_3-zTa_4$
S_{14}		$zO2_1-zO2_2+zO2_3-zO2_4$
S_{15}		$zO3_1-zO3_2$
S_{16}		zSr_1-zSr_2
	E_g	**$B_{1g}+B_{2g}$**
S_{17}	yTa_1-yTa_2	$yTa_1-yTa_2-yTa_3+yTa_4$ (B_{1g})
S_{18}	zTa_1-zTa_2	$zTa_1-zTa_2-zTa_3+zTa_4$ (B_{2g})
S_{19}	$yO2_1-yO2_2$	$yO2_1-yO2_2-yO2_3+yO2_4$ (B_{1g})
S_{20}	$zO2_1-zO2_2$	$zO2_1-zO2_2-zO2_3+zO2_4$ (B_{2g})
S_{21}	$yO1_1+zO1_1+yO1_2-zO1_2-yO1_3-zO1_3-yO1_4+zO1_4$	$yO1_1+zO1_1-yO1_2+zO1_2-yO1_3-zO1_3+yO1_4-zO1_4+yO'1_1-zO'1_1-yO'1_2-zO'1_2-yO'1_3+zO'1_3+yO'1_4+zO'1_4$ (B_{1g})
S_{22}	$yO1_1+zO1_1-yO1_2+zO1_2-yO1_3-zO1_3+yO1_4-zO1_4$	$yO1_1+zO1_1+yO1_2-zO1_2-yO1_3-zO1_3-yO1_4+zO1_4-yO'1_1+zO'1_1-yO'1_2-zO'1_2+yO'1_3-zO'1_3+yO'1_4+zO'1_4$ (B_{2g})
S_{23}	$yO1_1-zO1_1+yO1_2+zO1_2-yO1_3+zO1_3-yO1_4-zO1_4$	$yO1_1-zO1_1-yO1_2-zO1_2-yO1_3+zO1_3+yO1_4+zO1_4+yO'1_1+zO'1_1-yO'1_2+zO'1_2-yO'1_3-zO'1_3+yO'1_4-zO'1_4$ (B_{1g})
S_{24}	$yO1_1-zO1_1-yO1_2-zO1_2-yO1_3+zO1_3+yO1_4+zO1_4$	$yO1_1-zO1_1+yO1_2+zO1_2-yO1_3+zO1_3-yO1_4-zO1_4-yO'1_1-zO'1_1-yO'1_2+zO'1_2+yO'1_3+zO'1_3+yO'1_4-zO'1_4$ (B_{2g})
S_{25}	yLi_1-yLi_2	$yLi_1+yLi_2-yLi_3-yLi_4$ (B_{2g})
S_{26}	zLi_1-zLi_2	$zLi_1+zLi_2-zLi_3-zLi_4$ (B_{1g})
		B_{1g}
S_{27}		$xTa_1-xTa_2+xTa_3-xTa_4$
S_{28}		$xO2_1-xO2_2+xO2_3-xO2_4$
S_{29}		$xO3_1-xO3_2$
S_{30}		xSr_1-xSr_2
S_{31}		$yO1_1-zO1_1-yO1_2-zO1_2-yO1_3+zO1_3+yO1_4+zO1_4-yO'1_1-zO'1_1+yO'1_2-zO'1_2+yO'1_3+zO'1_3-yO'1_4+zO'1_4$
S_{32}		$yO1_1+zO1_1-yO1_2+zO1_2-yO1_3-zO1_3+yO1_4-zO1_4-yO'1_1+zO'1_1+yO'1_2+zO'1_2+yO'1_3-zO'1_3-yO'1_4-zO'1_4$
S_{33}		$yLi_1-yLi_2-yLi_3+yLi_4$
		B_{2g}
S_{34}		$yO1_1-zO1_1+yO1_2+zO1_2-yO1_3+zO1_3-yO1_4-zO1_4+yO'1_1+zO'1_1+yO'1_2-zO'1_2-yO'1_3-zO'1_3-yO'1_4+zO'1_4$
S_{35}		$yO1_1+zO1_1+yO1_2-zO1_2-yO1_3-zO1_3-yO1_4+zO1_4+yO'1_1-zO'1_1+yO'1_2+zO'1_2+yO'1_3-zO'1_3-yO'1_4-zO'1_4$
S_{36}		$zLi_1-zLi_2-zLi_3+zLi_4$
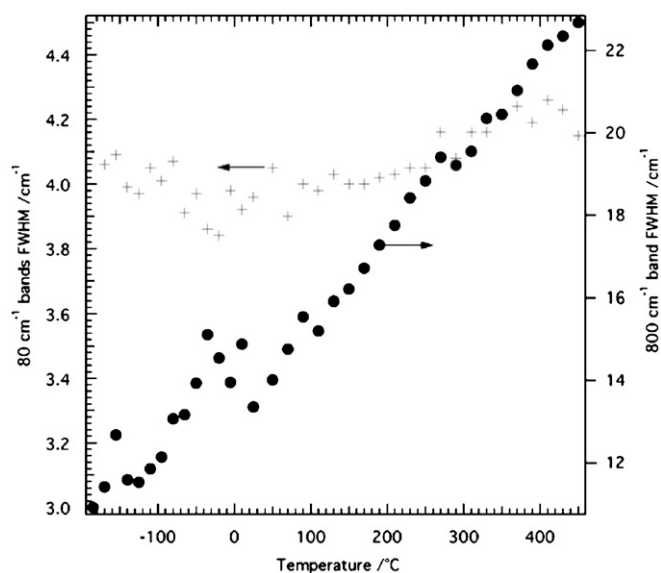
Fig. 12. Changes in the $80\,cm^{-1}$ Raman band full width at half maximum (FWHM) and in the $800\,cm^{-1}$ Raman band FWHM as a function of temperature.

5. Conclusion

A novel phase transition from orthorhombic to tetragonal symmetry was depicted for $Li_2SrTa_2O_7$, transition characterized by thermal X-ray and neutron diffraction and thermal Raman measurements. The progressive changes in the cell parameters, and in the normal mode wavenumbers, together with the absence of peak in the DTA curve indicate a second order phase transition occurring in the temperature range 210–250 °C.

At RT, both Raman spectroscopy results and neutron diffraction data indicate a $Cmcm$ structure. The disagreement between the results proposed by Floros [9] and us [8] in 1999 underlines the importance of the synthesis stage in order to study well organized samples, especially in the case of slight symmetry distortion. The orthorhombic distortion is clearly visible on the XRD pattern while the small octahedra tilting inside the perovskite layers is only depicted from neutron diffraction data and TEM study, as it is due to small displacements of the oxygen atoms. In 2006, similar phase transition ($Fmmm$ to $I4/mmm$) was published from XRD data for the layered perovskite $BaNd_2Mn_2O_7$ [21]. Taking into account our current study, it would be interesting to re-investigate the structure of $BaNd_2Mn_2O_7$ from neutron diffraction data and Raman spectroscopy. Moreover and as many

layered perovskite phases present octahedral tilting inside the perovskite blocks [22], we can reasonably think that such phase transition might be observed in these perovskites if high temperature data were collected. At $300\,^\circ C$, the neutron study allows to describe the structure of $Li_2SrTa_2O_7$ in the tetragonal $I4/mmm$ space group, result confirmed by the Raman study. Finally, it is worthy to note that the compound $Li_2SrNb_2O_7$ presents the same behavior, with a temperature transition close to $250\,^\circ C$, never observed until now.

Appendix A. Supplementary material

Supplementary data associated with this article can be found in the online version at doi:10.1016/j.jssc.2008.10.029.

References

[1] M. Dion, M. Ganne, M. Tournoux, Rev. Chim. Miner. 23 (1986) 61;
A.J. Jacobson, J.W. Johnson, J.T. Lewandowski, Inorg. Chem. 24 (1985) 3727;
J. Gopalakrishnan, V. Bhat, Inorg. Chem. 26 (1987) 4299;
N.S.P. Bhuvanesh, M.P. Crosnier-Lopez, H. Duroy, J.L. Fourquet, J. Mater. Chem. 10 (2000) 1685.
[2] K. Toda, S. Kurita, M. Sato, Solid State Ionics 81 (1995) 267.
[3] K. Shimizu, Y. Tsuji, T. Hatamachi, K. Toda, T. Kodama, M. Sato, Y. Kitayama, Phys. Chem. Chem. Phys. 6 (2004) 1064;
W. Yao, J. Ye, Chem. Phys. Lett. 435 (2007) 96.
[4] R. Seshadri, C. Martin, M. Herien, B. Raveau, C.N.R. Rao, Chem. Mater. 9 (1997) 270.
[5] G. Mangamma, V. Bhat, J. Gopalakrishnan, S.V. Bhat, Solid State Ionics 58 (1992) 303;
C.E. Tambelli, J.P. Donoso, C.J. Magon, A.C.D. Angelo, A.O. Florentino, M.J. Saeki, Solid State Ionics 136–137 (2000) 243.
[6] J.A. Schottenfeld, Y. Kobayashi, J. Wang, D.D. Macdonald, T.E. Mallouk, Chem. Matter 20 (2008) 213;
M.A. Bizeto, V.R.L. Constantino, Mater. Res. Bull. 39 (2004) 1811.
[7] M.P. Crosnier-Lopez, F. Le Berre, J.L. Fourquet, Z. Anorg. Allg. Chem. 628 (2002) 2049;
A. Snedden, K.S. Knight, P. Lightfoot, J. Solid State Chem. 173 (2003) 309.
[8] N.S.P. Bhuvanesh, M.P. Crosnier-Lopez, H. Duroy, J.L. Fourquet, J. Mater. Chem. 9 (1999) 3093.
[9] N. Floros, C. Michel, M. Hervieu, B. Raveau, J. Mater. Chem. 9 (1999) 3101.
[10] J. Rodriguez-Carvajal, Program FULLPROF.2K, Version 3.20, 2005, Institut Laüe-Langevin, Grenoble.
[11] W.H. Press, S.A. Teukolsky, W.T. Vetterling, B.P. Flannery, Numerical Recipes in C, second ed., Cambridge University Press, New York, NY USA, 1995.
[12] S. Ueno, N. Kamegashira, Powder Diff. 12 (1997) 103.
[13] M.P. Crosnier-Lopez, H. Duroy, J.L. Fourquet, Mater. Res. Bull. 34 (1999) 179.
[14] N.E. Brese, M. O'Keeffe, Acta Crystallogr. B 47 (1991) 192.
[15] K.S. Aleksandrov, J. Bartholomé, J. Phys. Condens. Matter 6 (1994) 8219.
[16] M.A. Subramanian, M.K. Crawford, R.L. Harlow, Mater. Res. Bull. 29 (1994) 645.
[17] H. Matsuhata, I. Nagai, Y. Yoshida, S. Hara, S.-I. Ikeda, N. Shirakawa, J. Solid State Chem. 177 (2004) 3776.
[18] G. Blasse, G.P.M. Van Den Heuvel, J. Solid State Chem. 10 (1974) 206.
[19] S.H. Byeon, S.O. Lee, H. Kim, J. Solid State Chem. 130 (1997) 110.
[20] P. Bouvier, G. Lucazeau, J. Phys. Chem. Solids 61 (2000) 569.
[21] J. Meng, H. Satoh, M. Ishida, N. Kamegashira, J. Alloys Compd. 408–412 (2006) 1182.
[22] T. Tokumitsu, K. Toda, T. Aoyagi, D. Sakuraba, K. Uematsu, M. Sato, J. Ceram. Soc. Jpn. 114 (2006) 795;
M. Caldes, C. Michel, T. Rouillon, M. Hervieu, B. Raveau, J. Mater. Chem 12 (2002) 473;
N. Shah, M.A. Green, D.A. Neumann, J. Phys. Chem. Solids 63 (2002) 1779;
H. Matsuhata, I. Nagai, Y. Yoshida, S. Hara, S.-I. Ikeda, N. Shirakwa, J. Solid State Chem. 177 (2004) 3776;
A.R. Armonstrong, P.A. Anderson, Inorg. Chem. 33-19 (1994) 4366;
G.H. Lander, P.J. Brown, J. Spalek, J.M. Honig, Phys. Rev. B 40 (1989) 4463;
U. Lehmann, Hk. Müller-Buschbaum, Z. Anorg. Allg. Chem. 470 (1980) 59.